HAL
open science

3D-printed scaffold combined to 2D osteoinductive coatings to repair a critical-size mandibular bone defect

M. Bouyer, C. Garot, P. Machillot, J. Vollaire, V. Fitzpatrick, S. Morand, J. Boutonnat, V. Josserand, G. Bettega, C. Picart

To cite this version:

M. Bouyer, C. Garot, P. Machillot, J. Vollaire, V. Fitzpatrick, et al.. 3D-printed scaffold combined to 2D osteoinductive coatings to repair a critical-size mandibular bone defect. Materials Today Bio, Elsevier, 2021, 11, pp.100113. 10.1016/j.mtbio.2021.100113 . hal-03247374

HAL Id: hal-03247374

https://hal.archives-ouvertes.fr/hal-03247374

Submitted on 7 Jun 2021

HAL is a multi-disciplinary open access archive for the deposit and dissemination of scientific research documents, whether they are published or not. The documents may come from teaching and research institutions in France or abroad, or from public or private research centers.

L'archive ouverte pluridisciplinaire **HAL**, est destinée au dépôt et à la diffusion de documents scientifiques de niveau recherche, publiés ou non, émanant des établissements d'enseignement et de recherche français ou étrangers, des laboratoires publics ou privés.

Materials Today Bio 11 (2021) 100113

Contents lists available at ScienceDirect

Materials Today Bio

journal homepage: www.journals.elsevier.com/materials-today-bio

3D-printed scaffold combined to 2D osteoinductive coatings to repair a critical-size mandibular bone defect

M. Bouyer [a,b,c,d,j], C. Garot [a,b,j], P. Machillot [a,b], J. Vollaire [c,e], V. Fitzpatrick [b], S. Morand [a,b,f], J. Boutonnat [g,h], V. Josserand [c,e], G. Bettega [c,e,f,**,k], C. Picart [a,b,i,*,k]

[a] CEA, CNRS, Université de Grenoble Alpes, ERL5000 BRM, IRIG Institute, 17 Rue des Martyrs, F-38054, Grenoble, France
[b] CNRS and Grenoble Institute of Engineering, UMR5628, LMGP, 3 Parvis Louis Néel, F-38016, Grenoble, France
[c] Université Grenoble Alpes, Institut Albert Bonniot, F-38000, Grenoble, France
[d] Clinique Générale d'Annecy, 4 Chemin de la Tour la Reine, 74000, Annecy, France
[e] INSERM U1209, Institut Albert Bonniot, F-38000, Grenoble, France
[f] Service de Chirurgie Maxillo-faciale, Centre Hospitalier Annecy Genevois, 1 Avenue de l'hôpital, 74370, Epagny Metz-Tessy, France
[g] Unité Médico-technique d'Histologie Cytologie Expérimentale, Faculté de Médecine, Université Joseph Fourier, 38700, La Tronche, France
[h] Département d'Anatomie et Cytologie Pathologique, Institut de Biologie et de Pathologie, Centre Hospitalier Universitaire de Grenoble, France
[i] Institut Universitaire de France, 1 Rue Descartes, 75231, Paris Cedex 05, France

ARTICLE INFO

Keywords:
Scaffold
Bone morphogenetic protein 2 (BMP-2)
Tissue engineering
3D printing
Bone regeneration
Critical-size bone defect

ABSTRACT

The reconstruction of large bone defects (12 cm^3) remains a challenge for clinicians. We developed a new critical-size mandibular bone defect model on a minipig, close to human clinical issues. We analyzed the bone reconstruction obtained by a 3D-printed scaffold made of clinical-grade polylactic acid (PLA), coated with a polyelectrolyte film delivering an osteogenic bioactive molecule (BMP-2). We compared the results (computed tomography scans, microcomputed tomography scans, histology) to the gold standard solution, bone autograft. We demonstrated that the dose of BMP-2 delivered from the scaffold significantly influenced the amount of regenerated bone and the repair kinetics, with a clear BMP-2 dose-dependence. Bone was homogeneously formed inside the scaffold without ectopic bone formation. The bone repair was as good as for the bone autograft. The BMP-2 doses applied in our study were reduced 20- to 75-fold compared to the commercial collagen sponges used in the current clinical applications, without any adverse effects. Three-dimensional printed PLA scaffolds loaded with reduced doses of BMP-2 may be a safe and simple solution for large bone defects faced in the clinic.

1. Introduction

To date, autologous bone graft remains the major clinical solution to treat extensive bone loss and trauma [1], but it is hampered by several drawbacks, including limited availability, pain for the patient, additional healing time, and donor site morbidity. Tissue engineering using synthetic scaffolds, bioactive factors, and/or stem cells offers alternative therapeutic strategies and holds promise for bone regeneration [2], but the repair of large bone defects (around 5 cm^3) remains challenging [3]. In particular, for large bone defects, a structural synthetic scaffold may not be enough to support complete regeneration. Ceramics, notably composites of hydroxyapatite (HAP) and tricalcium phosphate (TCP) are the most biomimetic scaffolds [4], but are brittle and exhibit some variable biodegradability. Besides, they induce a basic level of bone formation [5]. Metals such as titanium are interesting for their mechanical properties [6] but can yield to stress shielding and are not biodegradable. The use of polymers has expanded, in view of their versatility, tunable mechanical properties, and biodegradability. To date, polycaprolactone (PCL) and polylactic acid (PLA) derivatives are the most widely used in bone tissue engineering [7].

Very interestingly, recent developments in additive manufacturing enable the design of custom-made three-dimensional (3D) architectured scaffolds that can be adapted to the defect size [8] and are easier to implement from a regulatory perspective [9]. Polymers are particularly

* Corresponding author.
** Corresponding author.
E-mail addresses: gbettega@ch-annecygenevois.fr (G. Bettega), catherine.picart@cea.fr (C. Picart).
[j] Co-first authors.
[k] Co-last authors.

https://doi.org/10.1016/j.mtbio.2021.100113
Received 1 February 2021; Received in revised form 20 April 2021; Accepted 24 April 2021
Available online 4 May 2021
2590-0064/© 2021 Published by Elsevier Ltd. This is an open access article under the CC BY-NC-ND license (http://creativecommons.org/licenses/by-nc-nd/4.0/).

well-suited for additive manufacturing of scaffolds [10]. They can be manufactured in the form of filaments and 3D printed using several techniques, including fused deposition modeling (FDM) [2,11]. The 3D architectured scaffold plays the role of a space filler that should be mechanically stable enough to enable bone ingrowth inside the pores of the scaffold. However, for large defect areas, a structural scaffold may not be enough to support complete regeneration.

In these cases, stem cells or exogenous factors can be added to the scaffold to enhance regeneration [12]. Using stem cells in combination with scaffolds appears to have potential because of their secretion of factors [13], but is more complicated to set up because different steps are required to harvest the cells from the patients, expand them in culture, and finally implant them back into the patient. As an alternative to stem cell implantation, the use of growth factors aims to recruit stem cells directly to the site of implantation. So far, bone morphogenetic protein 2 (BMP-2) has been the most widely studied clinically approved protein because of its ability to directly target BMP receptors at the cell surface and trigger stem cell differentiation in bone [14,15]. BMP-7 has also been used in combination with TCP/PCL scaffolds [5]. The challenge is to optimize the dose of BMPs to avoid possible side-effects [12,16] that can lead to inflammation and ectopic bone [17]. Recently, a BMP/activin A chimera (BV-265) has been developed with increased receptor binding [18]. Used in a composite matrix made of HAP granules and collagen I, BV-265 improved bone repair in non-human primate bone defect models, and allowed a 30-fold decrease in dose compared to BMP-2.

As an alternative to the incorporation of BMPs inside a carrier, surface coatings appear interesting [19,20] in that they enable to decouple the 3D scaffold architecture from the two-dimensional (2D) osteoinductive coatings. In our previous study [21], we showed that it is possible to repair a critical-size femoral bone defect in rats by combining a polymeric scaffold (3D hollow tube) with an osteoinductive surface coating using a polyelectrolyte film coating as a BMP-2 carrier.

An important step toward the clinical translation of a tissue-engineered construct is its preclinical testing on critical-size bone defects in large animals [2], which are needed to repair large bone volume defects (typically bone defects with a volume above 5 cm^3). To date, preclinical models still need to be improved [22] and are limited when it comes to the clinical translation of results [3,22]. Less than 13% of the studies are performed in large animals (sheep, goat, dog, and pig) and the vast majority do not use skeletally mature large animals [3].

Here, we designed a 3D polymeric scaffold made of clinical-grade PLA combined with an osteoinductive surface coating containing a tunable dose of BMP-2 to repair a critical-size bone defect in minipig mandibles on mature animals. This choice of animal model is significant, as it is physiologically close to humans. We designed and printed the 3D scaffold to fit a parallelepipedal volumetric bone defect of 12 cm^3, which corresponds to the largest bone defect studied to our knowledge. We coated its surface with a polyelectrolyte film as a BMP-2 carrier, which enables to deliver a tunable dose of BMP-2 locally, from the surface of the scaffold. BMP-2 doses were reduced in comparison to the clinically approved collagen sponge. The film-coated architectured scaffolds were implanted in a full-thickness mandibular bone defect for 3 months. They induced bone growth inside the pores of the scaffold in a homogeneous manner. Bone repair was BMP-2 dose-dependent and was as good as the autograft control, demonstrating the potential of such implants. These results support further evaluations of these new osteoinductive medical devices in human bone repair clinical trials.

2. Materials and methods

2.1. PLA scaffold preparation, polyelectrolyte multilayer film coating

Parallelepipedal 4 × 3 × 1 cm^3 biodegradable and bioresorbable scaffolds made of clinical-grade poly(L-lactide) (PLA, Poly-Med, Inc, Lactoprene® 100 M Monofilament 1.75 mm) were fabricated by FDM (3DXP - One). PLA filaments of ~400 μm in diameter and 200 μm in height were deposited following a +45°/-45° pattern with an interspacing distance of ~2 mm. The melting temperature for PLA 3D printing was 190 °C. Scaffolds had a porosity of 85%, with fully interconnected pores. After their fabrication and before their coating with polyelectrolyte films, the scaffolds were stored away from moisture in a desiccator with a silica gel.

To render the scaffolds osteoinductive, they were coated with polyelectrolyte films made of 24 alternating bilayers of poly(L-lysine) (PLL, Sigma, France) and hyaluronic acid (HA, Lifecore, USA), as previously described [21]. Briefly, the polyelectrolyte films were deposited layer-by-layer with a DR3 dip-coating robot (Riegler & Kirstein GmbH). A first layer of poly(ethyleneimine) (PEI, Sigma-Aldrich, France) was deposited by hand using a concentration of 5 mg/mL, followed by alternated layers of HA at 1 mg/mL and PLL at 0.5 mg/mL using the robot. The film crosslinking level was controlled by incubating the coated scaffolds in 30 or 70 mg/mL 1-ethyl-3-(3-dimethylaminopropyl)carbodiimide (EDC, Sigma, France). The film crosslinking level has an effect on the film stiffness, as shown in previous studies [23], EDC30 films being softer than EDC70 films. After UV sterilization of the film-coated scaffolds, BMP-2 (InductOs, Medtronic) was postloaded in the polyelectrolyte films at increasing loading concentrations of 20, 50, or 110 μg/cm^3, as previously described [21,24]. Finally, the osteoinductive scaffolds were rinsed, dried, and stored away from moisture in a desiccator with a silica gel until implantation.

2.2. Characterization of polyelectrolyte films and quantification of BMP-2 loading

Fluorescence microscopy and scanning electron microscopy (SEM) were used to characterize the film coating on the scaffolds. The effective coating of the air-dried polyelectrolyte films on the PLA scaffolds was assessed, after scratching the film with a needle, by SEM imaging with an FEI-Quanta 250 SEM-FEG in high vacuum at 15 keV using the Everhart–Thornley detector, as previously described [21,25]. Regarding fluorescence microscopy, the film-coated scaffolds were labeled with PLL^{FITC}, as previously described [26]. They were imaged using a Leica Macrofluo (Z16 Apo) fluorescence system using a 0.8X objective [25] and a Zeiss LSM 700 confocal microscope with a 10X objective to assess the homogeneous coating of the film.

The quantification of BMP-2 initially loaded in the polyelectrolyte film (deposited at the bottom of a 96-well microplate) was performed using a micro bicinchoninic acid assay (μBCA) test for low BMP-2 concentration (BMP20), whereas Nanodrop (Thermofisher) was used for higher concentrations. The concentration of BMP-2 in the loading solution was measured initially and then after 1 h and a half of incubation with the film-coated scaffold. The loaded amount, corresponding to the difference between these two values was also expressed as μg of protein per volume of scaffold (μg/cm^3). The quantity of BMP-2 effectively loaded onto the scaffolds was then deduced from this quantification (Table 1). The percentage of BMP-2 release in vitro after several washes with a physiological buffer (HEPES-NaCl) was determined by fluorescence spectrometry using BMP-2 carboxyfluorescein ($BMP\text{-}2^{CF}$).

2.3. In vivo critical-sized mandibular defect in minipigs

Mature female minipigs (lineage FBM 'down-sized,' age over 24 months) weighing 43–69.5 kg (mean 56.3 kg) were included in the study, which was approved by the animal ethics committee (N°*APAFIS#2876-2015111616474259 v2*). They were acclimated for 2 weeks before surgery and immediately accustomed to a smooth diet. Animals were given antibiotics 2 days before surgery (Amoxicillin and Clavulanic acid at 12.5 mg/kg). They were fasting almost 6 h before surgery. They were given pre-anesthetic medication in the form of Atropin 0.04 mg/kg, Azaperone 2 mg/kg by intramuscular injection, and Morphine 0.2 mg/kg by subcutaneous injection. Induction was performed with Tiletamine and Zolazepam (3–5 mg/kg). After oral intubation, anesthesia was maintained with

isoflurane. Animals were placed in supine position, the mandibular area was shaved and prepared with an iodine scrub. The mandibular body was exposed via a submandibular approach, leaving the periosteum on the bone. Bone resection was made with an oscillating saw, creating a full-thickness bone defect of 4 × 3 cm^2, including the periosteum, and penetrating the mandibular nerve canal. This resection was standardized using a phantom (an uncoated implant) to delimit the perimeter of resection. Two titanium reconstructive plates (Stryker 2.8 system, Freiburg, Germany) and twelve 2.7 mm diameter screws were used to stabilize the mandible by triangulation, before insertion of the implant in the defect (Stryker Leibinger GmbH & Co. Freiburg, Germany).

The implant was fixed on the titanium plate using 2/0 nylon stitches (Fig. 1). When a bone graft was used (positive control group), it was harvested from the iliac bone and fixed on the plate using two screws. The wound was closed in three layers without drainage. Both sides of the mandible were operated on in the same way.

Aftercare included Morphine 0.2 mg/kg injected subcutaneously according to clinical symptoms, a Fentanyl patch (50 μg/h) changed every 3 days for a period depending on the residual pain, antibiotics (Amoxicillin and Clavulanic acid 12.5 mg/kg) intraorally for 15 days, and Meloxicam 0.4 mg/kg for 3 days. The animals were followed up for 13 weeks in individual boxes. A veterinarian clinically evaluated the animals every day, three times per day during the first 2 days after surgery and once per day after. Analgesia was adapted according to symptoms. The animals were weighed once a week. Special attention was given to re-feeding and weight evolution. A complete blood analysis was performed before surgery, immediately after surgery, and once a week until euthanasia to assess an eventual general inflammatory reaction, or liver or kidney complications due to BMP or due to the resorption of the film and scaffold. Complete blood count, haptoglobin, and protein electrophoresis were measured to assess inflammation and hemostasis, whereas aspartate aminotransferases (ASAT), alanine aminotransferases (ALAT), alkaline phosphatase (ALP), gamma-glutamine transferase (CGT), and bilirubinemia were used to assess hepatic function. Serum creatinine and urea were quantified to assess renal function.

To optimize bone regeneration and the operating techniques, we performed a preliminary experiment in the minipig mandibles. We thus screened six conditions on three minipigs ($n = 1$): two crosslinking levels EDC30 and EDC70, two BMP-2 initial loading concentrations of 20 and 110 μg/cm^3, and two negative controls: i) empty defect to assess the critical size of the defect, and ii) film-coated scaffold (EDC70) without BMP-2. Each implant was randomized, implanted, and analyzed in a blind manner using computed tomography (CT) scans, the polyelectrolyte films being macroscopically indistinguishable. All analyses of experimental groups were also made in a blind manner.

In a second main experiment, two conditions were further studied in larger groups to perform statistical analysis (EDC30 was used for all groups). The lowest BMP-2 dose was increased from 20 to 50 μg/cm^3 to reach better bone regeneration ($n = 6$) and the highest BMP-2 dose was kept (110 μg/cm^3, $n = 5$). Another negative control was added (EDC30 film-coated scaffold without BMP-2), and bone autograft (BG; $n = 4$) was added as a positive control (see Table 2 for all experimental conditions).

Table 1
Quantification of the effective amount of BMP-2 loaded in the film-coated architectured scaffold.

	Targeted BMP-2 loading (μg/cm^3)	Total BMP-2 loaded (μg/implant)	Volumetric dose (μg/cm^3)
Preliminary experiment			
BMP20 ($n = 2$)	20	240	20
BMP110 ($n = 2$)	110	870	72.5
Second experiment			
BMP50 ($n = 6$)	50	326 ± 80	27
BMP110 ($n = 5$)	110	1000 ± 64	83

The total volume of the scaffold was 12 cm^3 and its effective surface measured by μCT was 144 cm^2. We targeted a BMP-2 loading (unit mass per unit of scaffold volume in μg/cm^3). The total amount of BMP-2 effectively loaded was calculated for each implant and reported in 'mass per volume of implant' (μg/cm^3).

After the last CT scan (day 91), the animals were euthanized by Pentobarbital injection. The skin around the mandible was examined attentively to notice eventual complications (fistulas, collection, inflammation, etc.).

Using the same submandibular approach, the titanium plates and screws were removed. On each side, a full-thickness sample of bone was removed using a surgical guide (Fig. 1) to get a margin of 1 cm native bone all around the initial implant. The bone pieces were fixed in 4% neutral-buffered formalin (Sigma, France) for 1 week at 4 °C.

2.4. CT scan and micro-CT analysis

Assessment of bone formation was made by CT scan after 30, 50, and 90 days in the preliminary experiment and after 16, 30, 51, and 91 days in the main experiment. These scans were acquired using a helicoidal BrightSpeed 16 scanner (General Electric) under gaseous anesthesia.

First, a CT-scan score was defined by the authors considering four criteria: the percentage of filling of the porous implant (F), the homogeneity of the newly formed bone (H), the ability to distinguish between cortical and cancellous bones (D), and the amount of 'ectopic' bone (bone outside the implant) (E). Each criterion was evaluated in a blind manner by four clinicians using a score between 0 and 4 (0 being the lowest grade and 4 the highest). Then, the global score (S) was calculated by each clinician and for each CT scan made during the follow-up period:

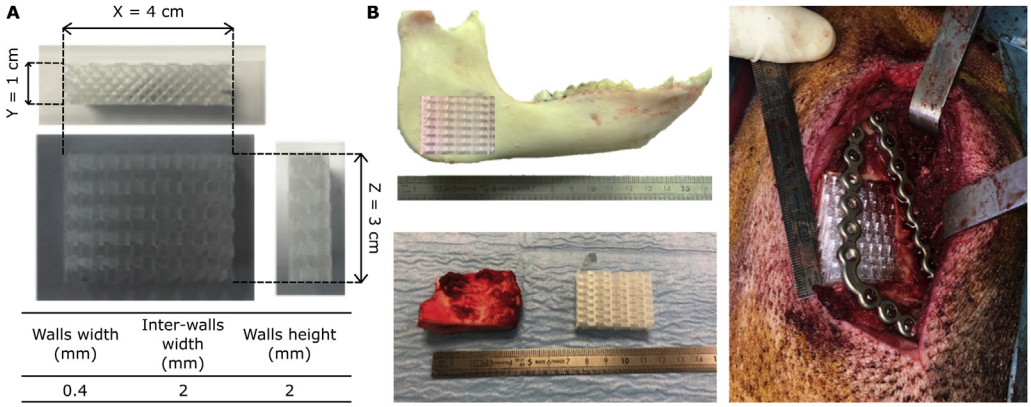

Fig. 1. 3D-printed PLA scaffold and experimental design of the in vivo experiments in the minipig mandible. (A) Parallelepipedal scaffolds (4 × 3 × 1 cm^3, total volume of 12 cm^3) were custom-made with clinical-grade PLA using a FDM 3D printer. PLA filaments of ~400 μm in diameter were deposited in a +45°/-45° pattern, with an interspacing of 2 mm, resulting in a scaffold with a porosity of 85% with fully interconnected pores. (B) Implantation in minipig mandibles. First, a bone defect was created into the minipig mandible and the bone was cut. Two 2.8 mm plates were fixed with 12 screws of length 2.7 mm and the implant was positioned in between with nylon stitches.

$$S = \frac{2F + 2H + D - E}{4} \quad (1)$$

More weight was given to the criteria F and H related to bone growth. Finally, the global score was represented as the mean score ± standard deviation (SD) of the four scores given by each clinician independently.

Second, a quantitative analysis of bone growth was performed using the software InVesalius 3 (Centro de Tecnologia da Informação Renato Archer, CTI). The volume of interest (VOI) was defined as the total volume of newly formed bone inside and around the bone defect. BG was used as a positive control. Based on the visual observations, we decided to segment and define two types of bones: poorly and highly mineralized. To quantify these two fractions, the VOI was segmented using a global threshold, namely between 230 and 629 HU for poorly mineralized bone and values >630 HU for highly mineralized bone. The volumes of the newly formed bone were expressed in cm^3. For the quantification of the bone volume outside the implant (named 'ectopic bone'), the VOI was adjusted to the volume of the scaffold. Then, the volume of bone inside this new VOI was subtracted from the total bone volume formed.

Third, micro-computed tomography (μCT) imaging was performed on fixed mandibular explants after 90 days, using high-resolution scanner (vivaCT 40, ScancoMedical, Switzerland), as previously described [21]. The acquisition parameters were set at 70 kV with an intensity of 114 μA, a 100-ms integration time, and an isotropic voxel size of 76 μm. The VOI was defined as the volume of the initial bone defect in the mandible ($4 \times 3 \times 1$ cm^3). Bone volume was determined after segmentation using threshold values (438–2730 mg HA/cm^3) and Gaussian filter (sigma 0.8, support 1). Bone mineral density (BMD, mg HA/cm^3) and the ratio of bone volume divided by total VOI (BV/TV) were calculated.

2.5. Bone homogeneity score

The implant of well-defined dimensions (4 cm × 3 cm × 1 cm, total volume TV of 12 cm^3) was taken as the region of interest (ROI). It was separated into 10 slices of equal thickness along each axis (X, Y, and Z). For each slice, the bone volume ratio (BVr = BV/TV) was calculated as the bone volume into one slice (BVs) divided by the volume of the slice of interest (corresponding to TV/10). This quantification was done for each axis (Fig. SI 9): the SD of BVr was calculated and the homogeneity score (HS) was defined as the sum of the three SDs over X, Y, and Z axes.

2.6. Histology and histomorphometry

The specimens were dehydrated in a graded series of alcohol and embedded in methylmethacrylate. Three slices in the XZ plane were cut with a laser microtome (TissueSurgeon, LLS ROWIAK GmbH, Hannover, Germany) [27] and stained with Sanderson's rapid stain and Van Gieson's staining. Bone appears in pink/orange, whereas mesenchymal tissue appears in blue or yellow. Slice thickness was 10–100 μm. Sections were imaged using a slide scanner (Aperio AT2, Leica Biosystems Imaging, Inc). Histological examination was performed by a pathologist using an Olympus BX51 microscope with transmitted or polarized light. The histomorphometry analysis was performed in a blind manner by three independent operators. The operators gave a visual approximation of the bone area to total area ratio since a systemic analysis was not possible because of the high differences in staining between the different sections, named hereafter S1, S2, and S3.

Table 2
Experimental conditions and total number of minipigs studied per group.

Film condition	BMP-2 targeted amount (in μg of BMP-2/cm^3 of scaffold)			
	BMP0	BMP20	BMP50	BMP110
No film	1 + 0	–	–	–
EDC30	0 + 1	1 + 0	0 + 6	1 + 5
EDC70	1 + 0	1 + 0	0 + 0	1 + 0
Bone autograft (BG, positive control)	0 + 4	–	–	–

For conditions studied in the preliminary experiment, $n = 1$. In the subsequent experiment, there were $n = 6$ implants loaded with EDC30 film and 50 μg/cm^3 BMP-2 and $n = 5$ implants loaded with EDC30 film and 110 μg/cm^3 BMP-2. In addition to these BMP-2 conditions, two negative control groups were added: i) defect left with no implant to confirm the critical size of the defect (no PLA scaffold, $n = 1$) and ii) film-coated PLA without BMP-2 ($n = 2$). A positive control group was added in the subsequent experiment (bone autograft, $n = 4$). On this table, the first number on the left of the "+" refers to the conditions of the preliminary experiment, whereas the second number, on the right, refers to the subsequent experiment.

2.7. Statistical analysis

OriginPro (OriginLab), Excel (Microsoft Office), and R for Mac OS X (R Foundation for Statistical Computing, CRAN) were used for all analyses. Data were expressed as mean ± SD. Non-parametric data were presented by median and interquartile range. Differences between groups were assessed by analysis of variance and Bonferroni post-hoc analysis or Student's t-test. Differences between groups at $p<0.05$ (*) and <0.01 (**) were considered as significant.

3. Results

3.1. 3D architectured scaffolds combined with an osteoinductive surface coating to repair a critical-size mandibular bone defect

Parallelepipedal scaffolds ($4 \times 3 \times 1$ cm^3, for a total volume of 12 cm^3) were made of clinical-grade PLA and custom-fabricated using FDM. The PLA filaments of ~400 μm in diameter were deposited following a +45°/-45° pattern with an interspacing of 2 mm, resulting in a scaffold porosity of 85% with fully interconnected pores (Fig. 1A) to enable the transport of fluids and nutrients in the core of the scaffold. This choice has been made after testing in laboratory several types of scaffold architectures (data not shown). The variations concerned their trabecular thickness from 1 to 2.5 mm, porosity from low to high porosity, and geometry. Their compression resistance, surface state, and fixation possibilities (suturing) were qualitatively tested. We also reasoned based on our preliminary study using film-coated poly(lactic-*co*-glycolic) acid PLGA hollow cylinders that showed that 3 mm diameter cylinders enabled bone formation inside the empty space of the cylinder [21].

As an implantation site, a large critical-size minipig mandibular bone defect (12 cm^3; Fig. 1B) was chosen because the pig mandible mimics the human mandible [28,29]. This was a full-thickness defect on the basilar border of the mandibular angle, scarifying the alveolar bundle. A posterior location was chosen because it has been shown that the extent of defect regeneration from spontaneous healing was significantly less in the posterior than in the anterior mandibular defects [30]. Buccal and vestibular periosteum were removed around the defect to avoid spontaneous ossification. In addition, the animals were mature, older than 24 months, without any remaining growth potential. This age was selected as our previous preliminary study on four minipigs aged 6–8 months had shown some spontaneous ossification of the defect spreading from the edges (data not shown). Thus, choosing animals older than 24 months ensured that bone maturation had occurred and that new bone formation would not result from the endogenous bone formation resulting from the animal growth. The implant was inserted in the defect and fixed using nylon stitches on the two thick titanium plates used to stabilize the mandible by triangulation; 12 screws fixed the plates (Fig. 1B).

The homogeneous coating of the scaffold by the polyelectrolyte film was visualized by fluorescent labeling of the film with PLL^{FITC} and imaged using a fluorescence macroscope (Fig. 2A) and confocal microscopy (Fig. 2B). As observed by SEM after scratching the film using a needle, the polyelectrolyte film fully coated the PLA filaments (Fig. 2C). The amount of BMP-2 initially loaded in the polyelectrolyte film and the percentage of BMP-2 released in vitro were determined by fluorescence

spectrometry using fluorescently labeled BMP-2 (Fig. 2D and E). This in vitro release study allowed having a general idea of the initial release, though the in vivo behavior may be different on the long term. The amount of BMP-2 adsorbed in the film increased with the initial concentration of BMP-2 in the loading solution before reaching a plateau. This plateau was reached faster for the EDC70 film (Fig. 2D), meaning that the EDC30 film was able to adsorb more BMP-2 than the EDC70 film. The amount of BMP-2 released from the film was higher for the EDC30 film: the maximum percentage of BMP-2 released from the film was ~50% for EDC30 films, compared to ~20% for EDC70 films (Fig. 2E). It thus appears that EDC30 films could adsorb and then release more BMP-2 than more crosslinked films.

3.2. A first preliminary experiment to validate the mandibular bone defect model and select the film coating conditions

Six different conditions ($n = 1$ for each condition) were initially screened to validate the bone defect model and optimize the selection of the film crosslinking level and BMP-2 loading. Two film crosslinking levels (EDC30 and EDC70) and two concentrations of BMP-2 (BMP20 and BMP110) were tested (Table 2). We chose these BMP-2 doses following a literature analysis, indicating that the studies were previously conducted in the range from 0.03 to 3 mg/cm^3 [16,44–47] and based on our previous studies in rat and rabbit [21,48]. Our aim was to reduce the BMP-2 dose compared to what was usually done. These concentrations, expressed in μg of BMP-2 per cm^3 of scaffold, were the targeted 'volumetric' concentrations of BMP-2. Knowing the effective surface of the scaffold (144 cm^2) and the amount of BMP-2 loaded in the polyelectrolyte film (Fig. 2D), the concentration of BMP-2 in the loading solution (in μg/mL) into which the scaffold was dipped was defined. The amounts of BMP-2 that were effectively loaded in the film-coated 3D scaffolds were quantified (Table 1). Two negative controls were added: an empty defect without any implant, and a defect with a film-coated implant (crosslinking level EDC70) but without BMP-2.

The animals were in good health. There was no postoperative infection, implant failure, or sign of blood disorder. All the surgical procedures

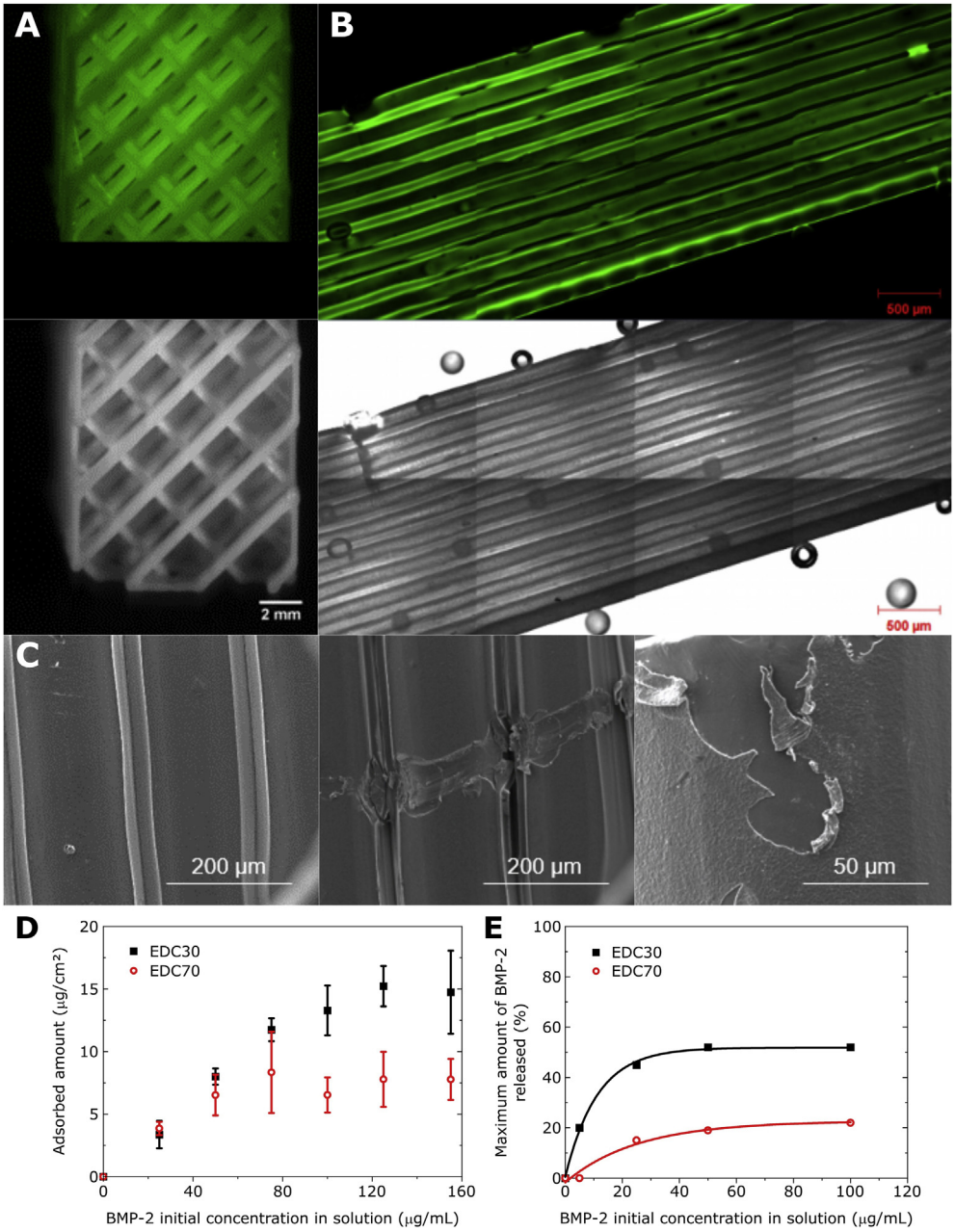

Fig. 2. Imaging of the film-coated 3D-printed PLA scaffolds. (A) Macroscope imaging of a $(PLL/HA)_{24}$ film-coated implant using fluorescence and phase-contrast imaging modes. (B) Confocal imaging of a section to visualize the film-coated struts of the scaffold. (C) SEM imaging of the struts and of a scratch made using a needle, to assess the presence of the film. (D) Quantification using μBCA of BMP-2 loading in $(PLL/HA)_{24}$ films as a function of the initial BMP-2 concentration in the loading solution for two crosslinking levels EDC30 and EDC70. (E) Quantification of the BMP-2 release (expressed in %) as a function of the initially loaded BMP-2 concentration, for two crosslinking levels EDC30 and EDC70.

were uneventful and there were no surgical complications. For one implant, it was necessary to recut the anterior border of the defect to improve the fit of the implant. All the titanium plates were stable and fixed to the native bone (no loosening). During explantation, it was impossible to macroscopically identify the implant from bone reconstruction or scar tissue. The complete blood analysis performed on three different minipigs did not reveal any abnormality (Fig. SI 1). We concluded that the scaffold with or without the film and/or BMP-2 did not cause a general inflammation, a hepatic reaction, or a renal function impairment.

CT scans were acquired during the follow-up period (Fig. SI 2). For each acquisition, a CT-scan score was given in a blind manner and independently by four clinicians (Fig. 3A and B). Bone grafts were not scored because bone homogeneity and cortical/cancellous differentiation would not change during the study and because they did not produce ectopic bone. All BMP groups exhibited bone regeneration, regardless of the crosslinking level of the film and the BMP-2 loading concentration, whereas the negative controls did not show any bone formation (Fig. 3B and Fig. SI 2). The CT-scan scores were plotted as a function of time and fitted an exponential function. The CT-scan score was used to calculate a plateau value (B_{max}) and a characteristic time to reach the plateau (τ), by fitting an exponential function to the experimental data [21]. For the EDC30 films (Fig. 3A), the scores steadily increased before reaching B_{max}, which was higher for the BMP110 than for BMP20 (4.8 ± 0.4 vs. 1.4 ± 0.0, respectively). τ was approximately 2.6 times faster for the lower dose than for the higher dose (21 ± 2 days vs. 55 ± 10 days). In contrast, for the EDC70 films, the exponential fit to the data was poor for the highest BMP-2 concentration, and there was no clear dose-dependent trend (Fig. 3B). For the lower BMP-2 dose, B_{max} was at 3.3 ± 0.4 and τ was 25 ± 10 days. These data indicate that bone repair is BMP-2 dose-dependent with EDC30 films but not with EDC70 films where scores are similar for BMP20 and BMP110 conditions. With the two film crosslinking level, the lower dose leads to a faster bone repair.

The quantification of the total regenerated bone volumes from the CT images for the different time points (D29, D50, and D90) confirmed the BMP-2 dose-dependence of bone repair for the EDC30 films and not for the EDC70 films (Fig. 3C). The amount of poorly mineralized bone and highly mineralized bone were also plotted (Fig. SI 3). The slopes of the linear fits were higher for the highly mineralized part, suggesting that this type of bone has more influence on the total bone volume than the poorly mineralized one.

μCT scans were acquired after explantation of the scaffolds. They were used to calculate the total bone volume (BV) and the BMD for all samples (Fig. SI 4). After 3 months, BV also exhibited a clear BMP-2 dose-dependence with EDC30 films but not with EDC70 films, while the BMD was rather stable. The μCT imaging of the EDC70 films confirmed that there was no visible BMP-2 dose-dependence for this film condition (Fig. SI 5).

The associated histological examination performed by a pathologist showed no sign of foreign body reaction (Fig. SI 6). For the low BMP-2 dose loaded on an EDC30 film-coated scaffold, very little new bone (NB) was formed and mesenchymal tissue (m) was largely observed (Fig. SI 6A). In contrast, the condition EDC30/BMP110 showed high bone formation with Haversian canals (*) and blood vessels already formed (Fig. SI 6B). The film-coated implant without BMP-2 showed no bone formation and only mesenchymal tissue could be observed (Fig. SI 6C). For the EDC70 film-coated implants, and independently of the BMP-2 dose, the histological sections showed bone tissue in formation (some mesenchymal tissue remained), with blood vessels and some Haversian canals already formed (Fig. SI 6D and E), proving that the bone was becoming more and more mature as it was growing. The quantitative histomorphometric analysis of bone area over total area (BA/TA) confirmed a clear BMP-2 dose-dependence of bone repair for the EDC30

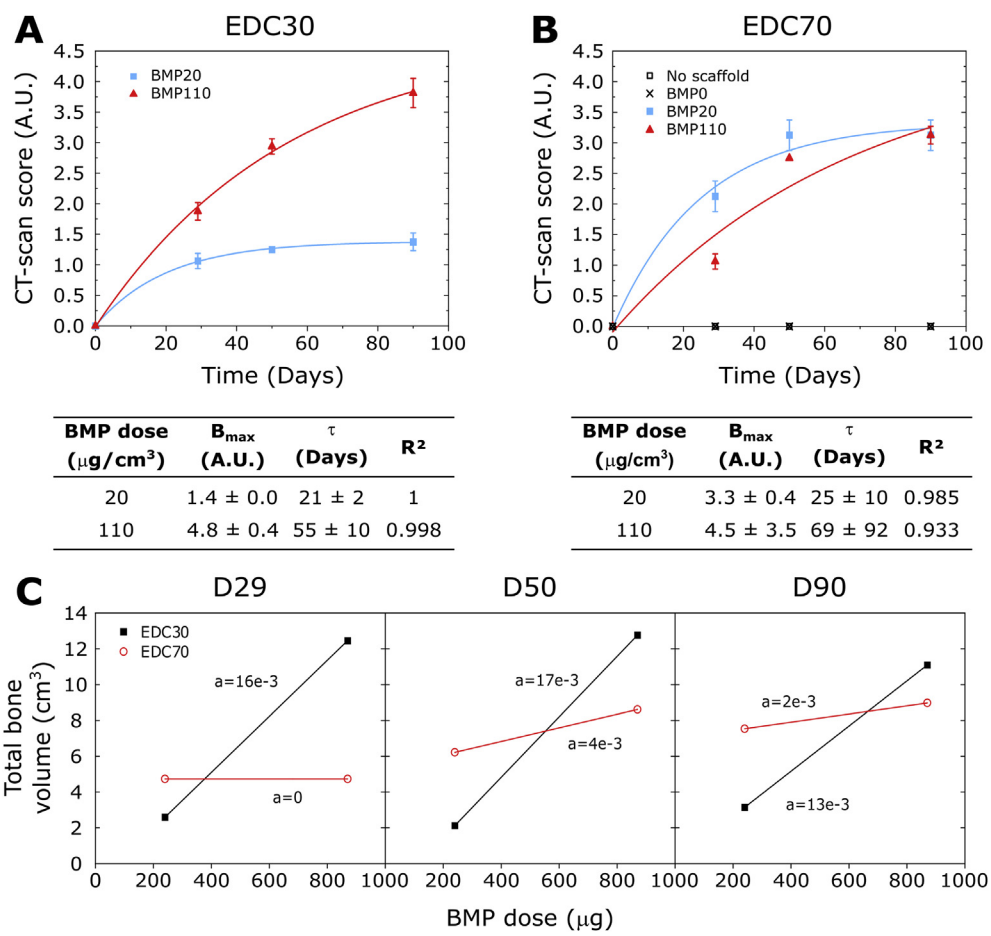

BMP dose (μg/cm³)	B_{max} (A.U.)	τ (Days)	R^2
20	1.4 ± 0.0	21 ± 2	1
110	4.8 ± 0.4	55 ± 10	0.998

BMP dose (μg/cm³)	B_{max} (A.U.)	τ (Days)	R^2
20	3.3 ± 0.4	25 ± 10	0.985
110	4.5 ± 3.5	69 ± 92	0.933

Fig. 3. Kinetic quantification of bone formation using CT scans obtained for the preliminary experiment with two crosslinking levels and two BMP-2 doses. EDC30 and EDC70 films loaded with BMP-2 doses (20 and 110 μg/cm^3 of scaffold corresponding to a total dose of 240 and 870 μg per implant, respectively) were compared. Two negative controls were added: empty defect (no scaffold) and film-coated implant without BMP-2. (A, B) CT-scan scores (mean of the global scores (S) given by the four clinicians ± SD) calculated from the CT scans as a function of time, and corresponding exponential fits to the data (red and blue lines) for the (A) EDC30 and (B) EDC70 groups. The plateau value (B_{max}), characteristic time (τ) deduced from the fits, and fit quality R^2 are given in the corresponding tables. (C) Total bone volume as a function of time (D29, D50, and D90) and as a function of the BMP-2 dose expressed in total dose per implant (in μg), for the two crosslinked films EDC30 and EDC70. Lines have been added to guide the eye.

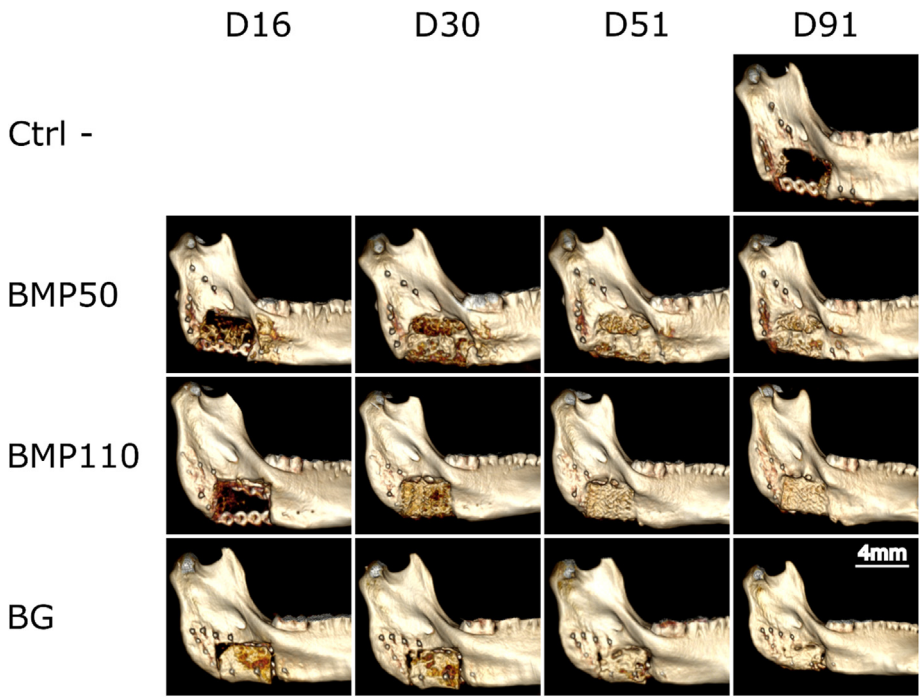

Fig. 4. Representative 3D reconstructions of the CT scans showing the kinetics of bone regeneration for four representative conditions: negative control (Ctrl -, film-coated scaffold without BMP-2 in the film), film-coated scaffold with a low BMP-2 dose (BMP50) and a high BMP-2 dose (BMP110), and BG. Scale bar is 4 mm.

films with a BA/TA ratio of 1.5 ± 1% for BMP20 and 40.8 ± 1.4% for BMP110 (Fig. SI 6F). Surprisingly, BA/TA significantly decreased with the BMP-2 dose for the EDC70 films (25.8 ± 3.8% for BMP20 vs. 12.5 ± 1.5% for BMP110).

Altogether, our results established the critical size of the mandibular bone defect, the difference in bone repair kinetics depending on the BMP-2 dose, and the influence of the film crosslinking level on the amount of newly formed bone. A clear BMP-2 dose-dependence was evidenced for the EDC30 films. This first preliminary experiment allowed to optimize our film coating parameters for the second main experiment.

3.3. The second main experiment shows that the BMP-2 dose influences the bone repair kinetics and the amount of highly mineralized bone

In view of the results of the preliminary experiment showing that BMP20 lead to only little bone formation and EDC70 induced lower bone regeneration, we decided to pursue the next study with only EDC30 films and increased the lowest BMP-2 dose from 20 to 50 μg/cm^3. The experiments were next repeated with more minipigs per condition (Table 2) to assess quantitatively the effect of BMP-2 dose. The highest dose BMP110 was kept ($n = 5$) and BMP50 was added ($n = 6$). BGs were added as a positive control ($n = 4$), and a film-coated scaffold without BMP-2 as a negative control (EDC30 film). An additional earlier time point (D16) was also added for the CT-scan acquisitions.

Once again, there was no surgical complication. In two cases, the BG was in two pieces because of the small size of the iliac bone, but in all cases, the defect was completely filled. In two cases (BG), a small serous collection was found around the implant, and in one case (high dose of BMP-2), a small suppurated collection with a cutaneous fistula appeared at D90.

Fig. 4 shows 3D reconstructions of CT scans over time for the BG, the

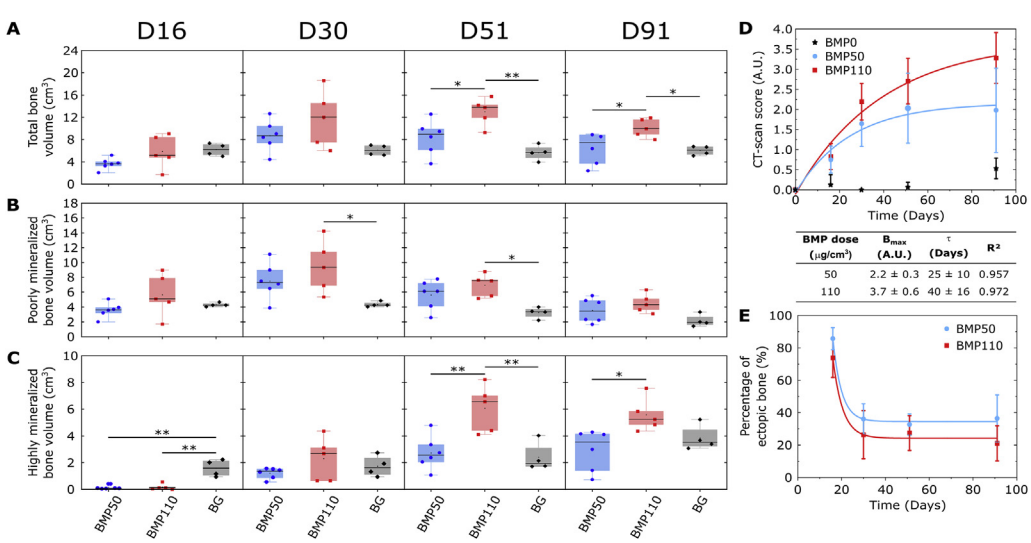

Fig. 5. Quantitative analysis of the kinetics of bone formation followed by CT for EDC30 films loaded with two BMP-2 doses. The film-coated scaffolds were loaded with BMP-2 at 50 ($n = 6$) and 110 μg/cm^3 ($n = 5$) and their bone regenerative capacity was compared to bone autograft (BG; $n = 4$). (A–C) Box plot representations of the total bone volume (A), poorly mineralized (B), and highly mineralized bone volumes (C) as a function of the BMP-2 dose BMP50 vs. BMP110 in comparison to BG. (D) CT-scan scores as a function of time and corresponding exponential fits to the data (colored lines) for EDC30 films; corresponding plateau value (B_{max}), characteristic time (τ) deduced from the fits, and fit quality R are given in the table. (E) % of bone outside the implant (named 'ectopic bone') as a function of time for BMP50 and BMP110. *p<0.05; **p<0.01.

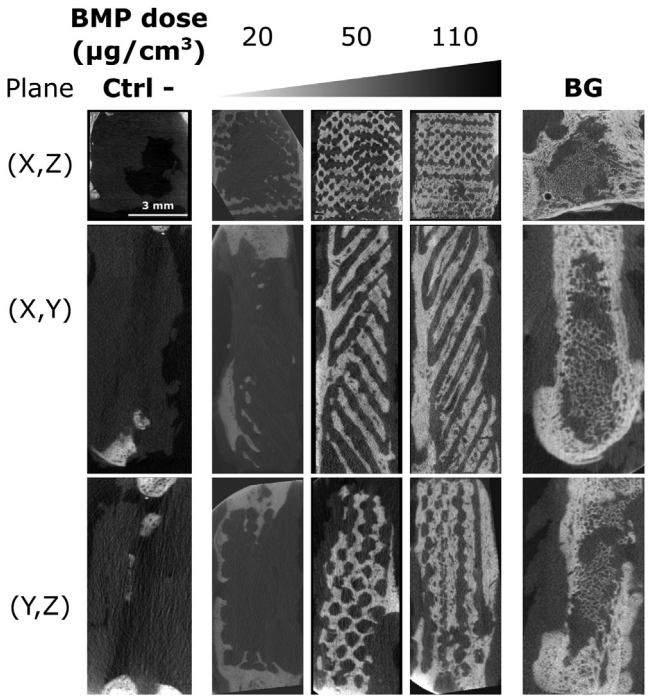

Fig. 6. Representative µCT images in the three sectional planes (see Fig. 1) for the film-coated scaffolds containing increasing doses of BMP-2 from 20 to 110 µg/cm^3. The negative control (Ctrl -, film-coated scaffold without BMP-2) is shown on the left, whereas the BG is shown on the right-hand side.

synthetic bone implant loaded with the two BMP-2 doses (BMP50 and BMP110), and the negative control (Ctrl -). At first sight, we observed that the BG mineralized over time but its total amount did not change. In contrast, the film-coated scaffolds induced bone repair over time, and mineralization was also visible. The total bone volume, the poorly mineralized and highly mineralized bone volumes were quantified from the CT scans (Fig. 5A–C). The total bone volume increased over time to reach a plateau, this increase being significantly higher for the highest BMP-2 dose condition than for the lower dose (Fig. 5A). The BG volume remained constant. The amount of poorly mineralized bone quickly increased with time for both BMP50 and BMP110, but with no statistical difference (Fig. 5B). In contrast, the amount of highly mineralized bone increased as a function of time, reaching a peak at D51 (Fig. 5C). It was significantly higher for BMP110 than for BMP50. These results confirmed what was already observed in the first preliminary experiment: bone regeneration is BMP dose-dependent and highly mineralized bone is more influenced by the BMP-2 dose than poorly mineralized bone.

The CT-scan scores were plotted as a function of time, and the data were fitted with an exponential fit (Fig. 5D). The score increased for the two BMP-2 doses, but again with different characteristics: B_{max} was lower for the scaffolds with BMP50 than that of the BMP110 (2.2 ± 0.3 vs. 3.7 ± 0.6). τ was 1.6-fold lower for BMP50 (25 ± 10 days) than for BMP110 (40 ± 16 days). Once again, this confirms the results from the preliminary experiment, showing that the amount of bone regenerated is higher with a higher BMP-2 dose while bone repair is faster for lower BMP-2 doses.

The part of the regenerated bone that was forming outside of the implant (Fig. 5E), called here 'ectopic bone,' was further analyzed. Initially high, the fraction of bone growing outside of the implant quickly reached a plateau value at around 28–35%, independently of the BMP-2 dose. We noted that the dispersion of the values was slightly higher for the high dose, and also slightly higher at the D91 endpoint. It can be concluded that the fraction of bone growing outside of the implant is low, independently of the BMP-2 dose.

The µCT analysis performed at day 90 after euthanasia of the minipigs was used to further analyze the newly formed bone (Figs. 6 and 7). µCT images are shown in the different planes ((X,Z), (X,Y), and (Y,Z)) for scaffolds containing increasing doses of BMP-2 (in µg/cm^3), taken from the experimental groups (Fig. 6). The negative control confirms the critical size of the mandibular bone defect, and the BG provides a positive reference value. For the lowest BMP-2 dose, bone formation was scarce. The amount of bone progressively increased when increasing the BMP-2 dose, and the newly formed bone entirely filled the pores of the 3D scaffold in a homogeneous manner for the highest dose. There was no sign of excessive ectopic bone formation, even at the highest dose. This was also visible on the 3D reconstructed µCT images (Fig. 7A and Fig. SI 7). The mean bone volume was higher for BMP110 (7.6 cm^3) than for BMP50 (4.8 cm^3) (Fig. 7B), and was also higher than for the BG reference but not significantly. In addition, bone regeneration was more dispersed with BMP50, with a variation coefficient of 34% compared to 13% for BMP110. When plotting all the experimental bone volumes as a function of the BMP-2 total dose per implant, a linear correlation was found (Fig. 7C), confirming the BMP-2 dose-dependence of bone regeneration. BMD was not significantly different for the different doses but was significantly higher for BMP50 than for BG (Fig. 7D). Furthermore, the amount of bone grown outside of the implant did not depend on the BMP-2 dose (Fig. SI 8), which confirmed what was found on CT scans. Finally, the HS of bone inside the scaffold was similar for BMP50 and BMP110 (Fig. 7E and Fig. SI9) and showed the homogeneous reconstruction of bone using the implants. These results showed that the 3D-printed PLA scaffolds coated with osteoinductive coatings and loaded with BMP-2 lead to a full bridging of the critical-size mandibular defect, with performances similar to BG. The best performances were achieved in the BMP110 group. The quantitative results of the CT scan analysis and the µCT analysis were compared to the CT-scan score (Fig. SI 10). The linear correlation between the quantification of the new bone volume using µCT acquisitions and the CT-scan score had a regression coefficient $R^2 = 0.82$ (Fig. SI 10B). This confirmed the usefulness of scoring by clinicians, which is a simple method to implement, leading to interesting results.

The histological examination (Fig. 8) revealed that when no BMP-2 was present, only mesenchymal tissue (m) was formed (Fig. 8A and B). With BMP50, the amount of new bone was low and mesenchymal tissue was visible (Fig. 8C and D). The presence of mature bone with a characteristic Haversian structure in BMP110 implants was evidenced (Fig. 8E–G). Imaging under polarized light (Fig. 8G) allowed a better visualization of the Haversian canals (highlighted by asterisks *) and the connections between osteocytes. Furthermore, the interface between the host bone and the newly formed bone was visible (Fig. 8H–J with dashed lines in Fig. 8I and J), since the host bone had a more lamellar structure than the newly-formed bone (Fig. 8J). Some bridges were visible between the two types of bones (white arrows in Fig. 8J), which may contribute to increasing the mechanical resistance of the newly formed bone. In some cases, especially for BMP110, the difference between native and new bone was not even distinguishable (data not shown). In the case of BG, host bone and grafted bone were in direct contact (Fig. 8K–M) or separated by mesenchymal tissue and new bone showed a Haversian structure (Fig. 8L and M). The bone area over total area (BA/TA in %) was quantified based on these images (Fig. 8N). In agreement with the CT and µCT quantifications, more bone was formed for BMP110, whose median value was similar with BG. The homogeneity of the newly formed bone inside the 3D architecture implant was quantified (Fig. 8O). Here again, bone formation was similar for the three sections of the sample, proving the homogeneity of bone formation. Finally, no local inflammation occurred because of the implant according to the absence of inflammatory cells and PLA degradation had not occurred yet (Fig. 8). These histological results confirmed the results from CT and µCT analyses showing that bone regeneration is BMP-2 dose-dependent. Moreover, BMP110 lead to similar bone formation as BG and new bone formed in this experimental group was mature, as assessed by the presence of Haversian canals.

Altogether, these data show that bone formation inside the 3D architectured scaffold is spatially homogeneous, and that there is a

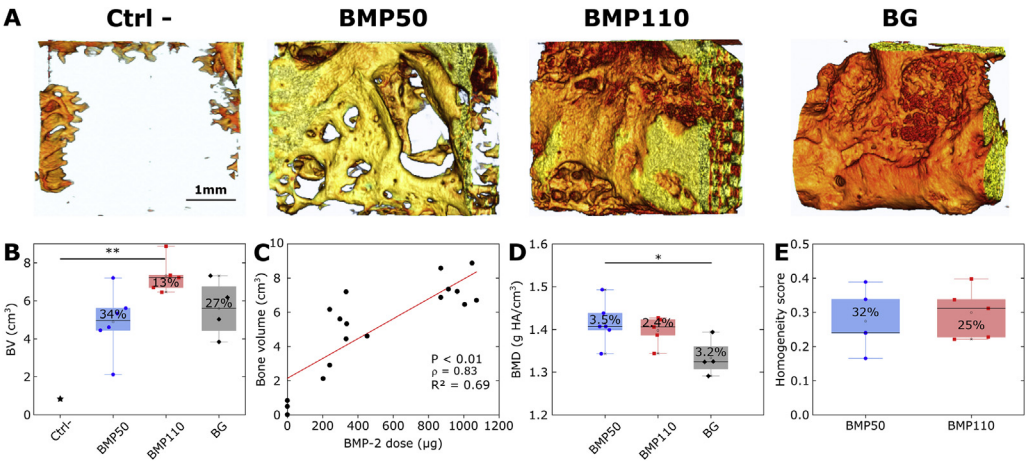

Fig. 7. Quantitative µCT analysis of bone formation at 3 months (D91), after explantation. (A) Representative 3D reconstructions obtained for: the negative control (EDC30 film-coated scaffold without BMP-2), film-coated scaffolds at BMP50 and BMP110, and bone autograft. (B) Box plot representation of the total bone volume as a function of the experimental group. (C) Total bone volume as a function of the total BMP-2 dose per implant. (D) Bone mineraldensity (BMD) as a function of the experimental group. (E) Homogeneity score measured for BMP50 and BMP110. In each box, the coefficient of variation of the data is given in %. *$p<0.05$; **$p<0.01$.

significant BMP-2 dose-dependent bone formation. BMP-2 mostly influences the formation of mineralized bone and does not induce the formation of ectopic bone.

4. Discussion

Before applying new osteogenic technologies in clinical practice, it is necessary to confirm their effectiveness in preclinical studies using critical-size bone defects in relevant animal models. A critical-size bone defect is a defect that does not spontaneously heal for the duration of the study. Our aim was to create a critical-size bone defect close to clinical situations, particularly in maxillofacial surgery where it is frequently needed to fill defects over 10 cm^3. Among the different animal models published, the pig is a very good candidate because the pig mandible mimics the human mandible in size, anatomy, form, and blood supply [29]. The bone physiology of the pig is very close to human bone physiology, with lamellar and Haversian structure. Several studies have reported on a mandibular defect in adult pigs. There is no real consensus on the critical size, it varied from 2 to 10 cm^3 depending on the location (tooth-bearing area or not, full-thickness or not, anterior or posterior area, periosteum preservation or not …) [31]. Otto and coworkers recently proposed a 6 cm^3 mandibular defect [32]. We carried out a full-thickness defect on the basilar border of the mandibular angle. The defect measured 3×4 cm^2, in a portion of mandible that was 1 cm thick, for a total defect volume of 12 cm^3. To the best of our knowledge, to date, there is no publication dealing with such a volume for a critical-sized bone defect in an animal model [3]. The buccal and vestibular periosteum was removed around the defect to avoid spontaneous ossification, and the age of the animals (24 months) precluded any growth potential as bone maturation had already occurred. The preservation of the alveolar ridge is another advantage of our model. The defect was created far from the teeth, and there was no opening into the oral cavity. This limits the risk for oral fistula and infection. The location of the defect at the mandibular angle permitted a very stable fixation with two reconstructive plates fixed with bicortical locked screws inserted into thick bone. We did not have mechanical complications (material loosening, plate or screw rupture) during the study. The negative control in our study (Figs. 3, 4 and 6) showed the validity of this critical-size bone defect model.

Long-term biodegradable polymers are interesting for bone tissue engineering applications and 3D printing to create porous scaffolds, because they can provide a temporary mechanical support while leaving sufficient space and time for the newly formed bone to grow. 3D-printed scaffolds are particularly suited for the repair of large bone defects. The family of polylactides (PLA, PGA) and PCL are the most widely used for bone tissue engineering [33]. 3D printing of PCL/HAP scaffolds using FDM has already been established [10,12,34]. It was shown that the porous scaffolds act as a guiding substrate to enable the formation of a structured fibrous network as a prerequisite for later bone formation [34], the HAP exhibiting osteoconductive properties. Later studies showed that this scaffold can be combined with an rhBMP-7 paste, and that BMP-7 accelerates the bone healing kinetics without changing the bone microstructure [35]. The same team used a critical-size sheep tibial model (30 mm long, 20 mm in diameter, i.e. a total volume of 6 cm^3 with a central empty space of 2.4 cm^3) to investigate whether a BMP-7 paste added inside the scaffold at two doses (1.75 and 3.5 mg) could influence bone growth. They did not see any BMP-7 dose-dependence [12]. As an alternative, we used PLA that is also widely used in orthopedic and maxillofacial surgery [7] because of its long-term biodegradability and modularity [36]. It also has interesting mechanical properties compared to PCL [7]. For the first time to our knowledge, we developed a 3D-printed PLA implant of clinical-grade using FDM. This fabrication process allowed for a complete control over the scaffold architecture. Indeed, compared to other widely used manufacturing methods such as freeze-drying, for example, the porosity can be controlled as well as the external shape of the scaffold [37]. Our previous studies had shown that the polyelectrolyte film can be deposited on PLGA cylinders [21] and PLA microcarriers [38], which was confirmed here on 3D-printed scaffolds. The PLA being inert, it does not provide osteoinduction and the osteoinductive properties are exclusively provided via the BMP-2-containing film coating. Thanks to the homogeneous surface coating of the 3D-printed scaffold by the film, bone formation was highly homogeneous inside all the pores of the scaffold (Figs. 6–8), and there was no general or local inflammatory reaction (Fig. 8 and Fig. SI 1). In addition, the PLA degrades over long term, typically from 6 months to 2 years [39], and no sign of degradation was found in the histological images (Fig. 8).

BMP-2 dose is a critical issue for clinical applications. It has been demonstrated that the osteogenic response is correlated to the dose of BMP-2 [40]. However, several studies showed that high doses are correlated with adverse effects [16,21], but it is difficult to find a consensus in the literature regarding the effective dose of BMP-2 to achieve the expected clinical results. Boden et al. [41] mentioned in their publication following a randomized clinical pilot trial for posterolateral lumbar fusion that the required dose (i.e. the concentration of growth factor expressed per volume of final collagen carrier matrix) to induce 100% consistent bone formation was substantially higher in non-human primates (1.5–2.0 mg/mL) than in rodents (0.2–0.4 mg/mL). James et al. [17] reviewed the side-effects of BMP-2 and noted that excessive concentrations of BMP-2 may be the most important factor contributing to the majority of adverse events: they noticed that increasing doses of BMP-2 do not necessarily result in higher fusion rates in spine procedures and long bone non-unions. These complications, described in clinical trials or in experimental studies, included postoperative inflammation (from benign seroma to life-threatening effects), ectopic bone formation,

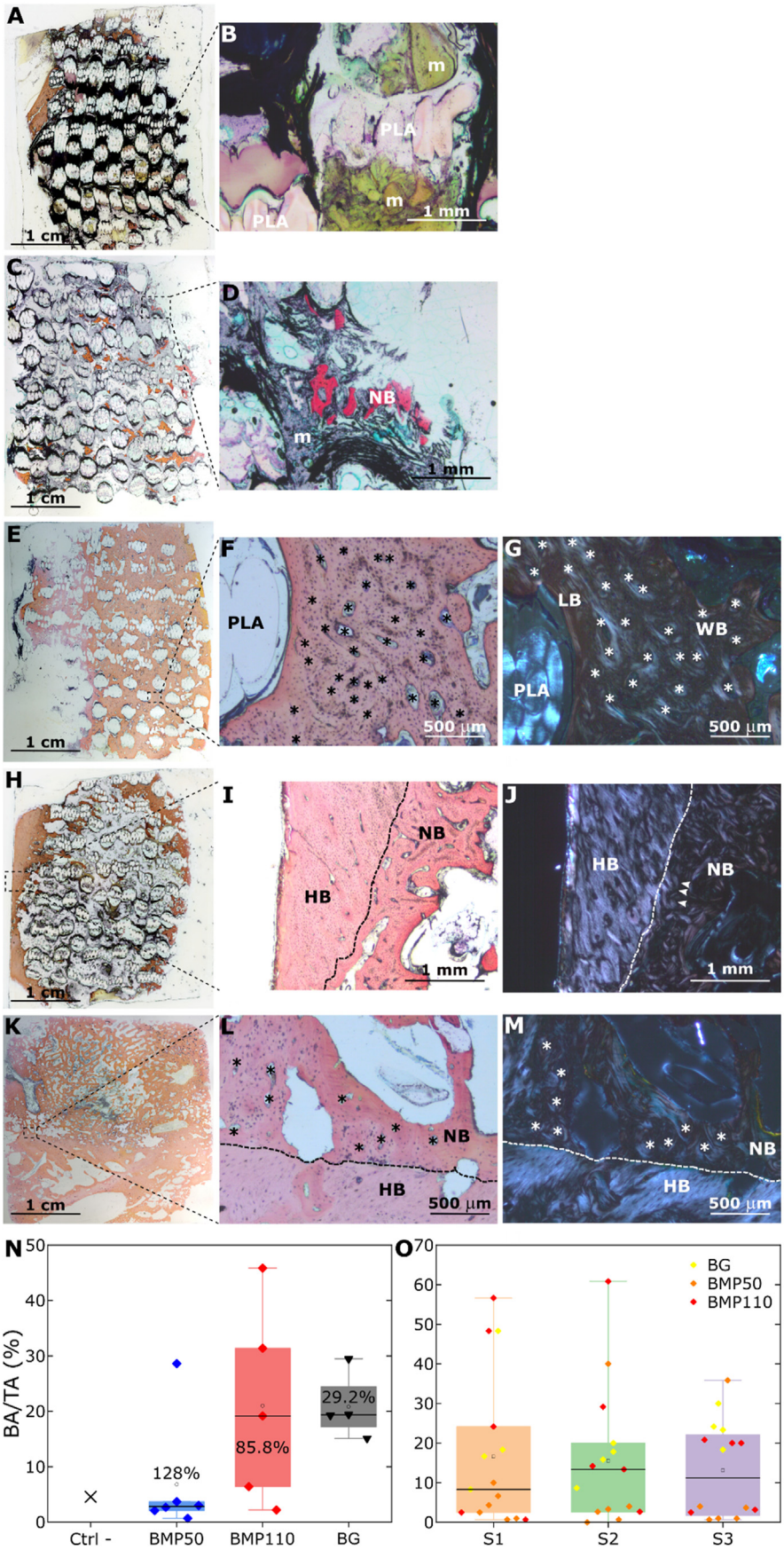

Fig. 8. Histological examination and histomorphometry analysis. (A–M) Representative histological sections to show the structure of the newly-formed bone in the different groups. (A, B) In the absence of BMP-2 in the film, only mesenchymal tissue (m) was formed. (A) Global section of the negative control (film-coated PLA scaffold at EDC30 without BMP-2). (B) Larger magnification of the box in (A) showing mesenchymal tissue around PLA struts. (C, D) With low BMP-2 dose (BMP50), new bone (NB) was formed along with mesenchymal tissue. (C) Global section of the BMP50 condition. (D) Larger magnification of the box in (C). (E–G) With higher BMP-2 dose (BMP110), the formation of new bone was evidenced. (E) Global section of the BMP110 condition where newly formed bone was present in high quantity (orange/pink staining). (F) Larger magnification of the box in (E) where the Haversian structure of newly formed bone was visible (Haversian canals are shown with an asterisk *), (G) and particularly evidenced under polarized light along with both lamellar (LB) and woven bones (WB). (H–M) Representative histological sections to show the contact between host bone and new bone. (H–J) Contact between host bone (HB) and new bone is shown for BMP110 condition with (H) the global section, (I) a larger magnification of the box in (H) showing the contact between host bone and new bone on a transmitted light image evidenced by a dashed line. (J) The HB/NB interface was clearly visible under polarized light, where bony bridges could be observed (white arrows). (K–M) Global section, transmitted and polarized light images for BG. The contact between HB and NB as well as the Haversian structure were evidenced. (N) Quantitative analysis of the bone area over total area (BA/TA). (O) Amount of bone over total area (BA/TA) inside each section of the implant (S1, S2, S3).

bone resorption and bone cyst formation, urogenital events (retrograde ejaculation, bladder retention), and wound complications [17,42,43]. The implication of BMP-2 in carcinogenesis is controversial. For all these reasons, it is important to reduce the dose of BMP-2 and to deliver it locally and progressively. Here, we considerably reduced the amount of BMP-2 with a dose of 240–1,000 μg per 12 cm^3 defect, which corresponded to 0.02–0.08 mg/cm^3 (1 mg/cm^3 is equivalent to mg/mL). This corresponds to a 20-fold (for BMP110) to 75-fold reduction compared to the commercially available collagen sponges, which are approved for a dose of 1.5 mg/mL. We chose these BMP-2 doses following a literature analysis, indicating that the studies were previously conducted in the range from 0.03 to 3 mg/cm^3 [16,44–47] and based on our previous studies in rat and rabbit [21,48]. Our aim was to reduce the BMP-2 dose compared to what was usually done.

Regarding the difference between EDC30 and EDC70 films in the BMP-2 dose-dependent bone regeneration (Fig. 3), we may hypothesize that it may be due to several reasons: i) the different stiffness of the EDC30 and EDC70 films, ii) the different loading of BMP-2 in the EDC30 and EDC70 films (Fig. 2D), the amount of BMP-2 loaded being higher for the EDC30 films at high BMP-2 concentrations, iii) the higher release for the EDC30 films as shown in Fig. 2E. iv) the fact that BMP-2 internalization by cells is higher for EDC30 than EDC70 [49]. To note, we did not quantify the amount of BMP-2 released in vivo but we know from previous in vitro published studies [21,25] that there is an initial burst release followed by a slower release. For a given BMP-2 loaded concentration, the amount of released BMP-2 is systematically higher for EDC30 films.

We did not notice adverse effects such as local inflammation, swelling, bone cysts, or bone resorption. In three cases, we noticed during the explantation a small seroma of less than 1 mL: two cases for the BG and one case for high-dose BMP-2. The amount of ossification outside the scaffold was small and independent of the BMP-2 dose (Fig. 6).

The visual scoring used by clinicians for the analysis of CT scans is a fine and simple way to evaluate bone regeneration. Although it can be considered as subjective, the number of independent operators (four in our case) and the fact that this is done in a blind manner prevented the risk of a biased view. Furthermore, the results correlated well to the quantitative analysis (Fig. SI 10). Another reason for using this score was to be close to the kind of evaluations that are usually conducted in the clinical routine. Similarly, the histomorphometry was conducted in a blind manner by three independent operators (Fig. 8I and J). Although this may result in over-estimation of the amount of new bone formation, it remains a simple and effective way to compare different conditions. Here, a systematic and purely objective evaluation was not possible. Again, the results were in accordance with the previous quantitative analyses (Figs. 5 and 6).

Our study opens perspectives for the clinical translation of these osteoinductive 3D-printed PLA scaffolds. First, the PLA used was clinical-grade and the film components are already approved by the US Food and Drug Administration (FDA) and the European Medicine Agencies (EMA) [21]. 3D printing is a cost-effective solution [10]. It has the potential to produce new medical products with unprecedented structural and functional designs, and its regulatory landscape is rapidly evolving [9]. The fact that the new synthetic graft proposed here is made of a 3D-printed scaffold and a 2D osteoinductive film coating containing BMP-2 offers several modularity possibilities in terms of scaffold design (dimensions, shape, architecture, porosity) and a precise control of BMP-2 dose delivered via the film coating. Regulations regarding the osteoinductive biomolecule, the BMP-2 growth factor, is also less difficult than that of stem cells [9], and is already clinically approved for several indications.

5. Conclusion

In summary, we engineered a 3D-printed scaffold made by FDM and coated with a biomimetic polyelectrolyte film loaded with BMP-2 to repair a new model of critical-size bone defect in minipig mandible. This bone defect model and volume >10 cm^3 is equivalent to various clinical applications in humans, showing the translation potential of our technology. The 3D architecture of the scaffold provided a guide for cells to grow inside the volumetric defect while the 2D osteoinductive coating allowed BMP-2 to trigger cell differentiation and bone regeneration. We showed that the BMP-2 dose delivered from the polyelectrolyte film significantly influenced the amount and maturity of regenerated bone with a clear BMP-2 dose-dependence for EDC30. The repair kinetics was also dose-dependent, with a slower kinetics for the high BMP-2 dose. CT scans, μCT acquisitions, and histological examinations proved the formation of mineralized and well-vascularized bone with high BMP-2 doses, whereas lower BMP-2 doses lead to less mineralized bone. In addition, the new bone formed homogeneously inside the scaffold, whatever the BMP-2 dose, and with little ectopic bone formation. This combination of a 3D-printed scaffold with a 2D osteoinductive coating opens perspectives in personalized medicine because 3D printing allows the customization of shape of implants and the biomimetic coating allows the controlled delivery of BMP-2 in space and time.

CRediT author contribution statement

MB: Conceptualization, Formal analysis, Investigation, Methodology, Visualization. **CG:** Formal analysis, Writing – original draft, Writing – review and editing, Visualization. **PM:** Investigation. **JV:** Formal analysis, Investigation, Writing – original draft. **VF:** Investigation. **SM:** Formal analysis. **JB:** Formal analysis. **VJ:** Formal analysis. **GB:** Conceptualization, Investigation, Methodology, Writing – original draft, Writing – review and editing, Supervision. **CP:** Conceptualization, Methodology, Writing – original draft, Writing – review and editing, Supervision, Funding acquisition.

Funding

The work was supported by the European Commission under the PF7 program (European Research Council grant BIOMIM GA259370 and Proof of Concept REGENERBONE 790435 to CP), by the 'Association Gueules Cassées' (contract n° 21-2016 and 10-2018) and by the French National Research Agency (ANR-18-CE17-0016, OBOE). Bone imaging systems were acquired thanks to France Life Imaging (FLI, ANR-11-INBS-44 0006). CP is a senior member of the Institut Universitaire de France whose support is acknowledged.

Data availability

The raw/processed data required to reproduce these findings cannot be shared at this time due to legal reasons. They are currently available upon request and will be deposited in a data repository.

Declaration of competing interest

The authors declare that they have no known competing financial interests or personal relationships that could have appeared to influence the work reported in this paper.

Acknowledgments

We thank the following for their contribution: Isabelle Paintrand (CNRS) and Jie Liu (Grenoble Institute of Technology) for help in the preparation of the samples, Jean-Luc Coll (Institute of Advanced Biosciences) and Remy Gerez (Institut Claude Bourgelat) for fruitful discussions, Heiko Richter and Birgitta Stolze (LLS Rowiak) for technical discussions, R Lartizien (Annecy Genenevois hospital) for help in the clinical score, Sebastien Schoumacker for help in 3D printing, Dorothée Palluy (Stryker) for providing the reconstruction plates and screws, and Sylvie Berthier (CHU-Grenoble Alpes) for her help in the quantitative histological analysis.

Appendix A. Supplementary data

Supplementary data to this article can be found online at https://doi.org/10.1016/j.mtbio.2021.100113.

References

[1] C. Laurencin, Y. Khan, S.F. El-Amin, Bone graft substitutes, Expet Rev. Med. Dev. 3 (1) (2006) 49–57.
[2] M. Woodruff, C. Lange, J. Reichert, A. Berner, F. Chen, P. Fratzl, J.J.-T. Schantz, D. Hutmacher, Bone tissue engineering: from bench to bedside, Mater. Today 15 (10) (2012) 430–432.
[3] S. Zeiter, K. Koschitzki, M. Alini, F. Jakob, M. Rudert, M. Herrmann, Evaluation of preclinical models for the testing of bone tissue-engineered constructs, Tissue Eng. C Methods 26 (2) (2020) 107–117.
[4] A. Oryan, S. Alidadi, A. Moshiri, N. Maffulli, Bone regenerative medicine: classic options, novel strategies, and future directions, J. Orthop. Surg. Res. 9 (1) (2014) 18.
[5] J.C. Reichert, A. Cipitria, D.R. Epari, S. Saifzadeh, P. Krishnakanth, A. Berner, M.A. Woodruff, H. Schell, M. Mehta, M.A. Schuetz, G.N. Duda, D.W. Hutmacher, A tissue engineering solution for segmental defect regeneration in load-bearing long bones, Sci. Transl. Med. 4 (141) (2012) 141ra93.
[6] X.P. Tan, Y.J. Tan, C.S.L. Chow, S.B. Tor, W.Y. Yeong, Metallic powder-bed based 3D printing of cellular scaffolds for orthopaedic implants: a state-of-the-art review on manufacturing, topological design, mechanical properties and biocompatibility, Mater Sci Eng C Mater Biol Appl 76 (2017) 1328–1343.
[7] Z. Sheikh, S. Najeeb, Z. Khurshid, V. Verma, H. Rashid, M. Glogauer, Biodegradable materials for bone repair and tissue engineering applications, Materials 8 (9) (2015) 5744–5794.
[8] A. Cheng, Z. Schwartz, A. Kahn, X. Li, Z. Shao, M. Sun, Y. Ao, B.D. Boyan, H. Chen, Advances in porous scaffold design for bone and cartilage tissue engineering and regeneration, Tissue Eng. B Rev. 25 (1) (2019) 14–29.
[9] L.M. Ricles, J.C. Coburn, M. Di Prima, S.S. Oh, Regulating 3D-printed medical products, Sci. Transl. Med. 10 (461) (2018).
[10] A. Youssef, S.J. Hollister, P.D. Dalton, Additive manufacturing of polymer melts for implantable medical devices and scaffolds, Biofabrication 9 (1) (2017), 012002.
[11] X. Liang, J. Gao, W. Xu, X. Wang, Y. Shen, J. Tang, S. Cui, X. Yang, Q. Liu, L. Yu, J. Ding, Structural mechanics of 3D-printed poly(lactic acid) scaffolds with tetragonal, hexagonal and wheel-like designs, Biofabrication 11 (3) (2019), 035009.
[12] A. Cipitria, J.C. Reichert, D.R. Epari, S. Saifzadeh, A. Berner, H. Schell, M. Mehta, M.A. Schuetz, G.N. Duda, D.W. Hutmacher, Polycaprolactone scaffold and reduced rhBMP-7 dose for the regeneration of critical-sized defects in sheep tibiae, Biomaterials 34 (38) (2013) 9960–9968.
[13] M.A. Brennan, A. Renaud, J. Amiaud, M.T. Rojewski, H. Schrezenmeier, D. Heymann, V. Trichet, P. Layrolle, Pre-clinical studies of bone regeneration with human bone marrow stromal cells and biphasic calcium phosphate, Stem Cell Res. Ther. 5 (5) (2014) 114.
[14] M.R. Urist, Bone - formation by autoinduction, Science 150 (3698) (1965), 893-&.
[15] V.E. Santo, M.E. Gomes, J.F. Mano, R.L. Reis, Controlled release strategies for bone, cartilage, and osteochondral engineering–Part II: challenges on the evolution from single to multiple bioactive factor delivery, Tissue Eng. B Rev. 19 (4) (2013) 327–352.
[16] J.N. Zara, R.K. Siu, X. Zhang, J. Shen, R. Ngo, M. Lee, W. Li, M. Chiang, J. Chung, J. Kwak, B.M. Wu, K. Ting, C. Soo, High doses of bone morphogenetic protein 2 induce structurally abnormal bone and inflammation in vivo, Tissue Eng. 17 (9–10) (2011) 1389–1399.
[17] A.W. James, G. LaChaud, J. Shen, G. Asatrian, V. Nguyen, X. Zhang, K. Ting, C. Soo, A review of the clinical side effects of bone morphogenetic protein-2, Tissue Eng. B Rev. 22 (4) (2016) 284–297.
[18] H.J. Seeherman, S.P. Berasi, C.T. Brown, R.X. Martinez, Z.S. Juo, S. Jelinsky, M.J. Cain, J. Grode, K.E. Tumelty, M. Bohner, O. Grinberg, N. Orr, O. Shoseyov, J. Eyckmans, C. Chen, P.R. Morales, C.G. Wilson, E.J. Vanderploeg, J.M. Wozney, A BMP/activin A chimera is superior to native BMPs and induces bone repair in nonhuman primates when delivered in a composite matrix, Sci. Transl. Med. 11 (489) (2019).
[19] W.J. King, P.H. Krebsbach, Growth factor delivery: how surface interactions modulate release in vitro and in vivo, Adv. Drug Deliv. Rev. 64 (12) (2012) 1239–1256.
[20] E. Migliorini, A. Valat, C. Picart, E.A. Cavalcanti-Adam, Tuning cellular responses to BMP-2 with material surfaces, Cytokine Growth Factor Rev. 27 (2016) 43–54.
[21] M. Bouyer, R. Guillot, J. Lavaud, C. Plettinx, C. Olivier, V. Curry, J. Boutonnat, J.L. Coll, F. Peyrin, V. Josserand, G. Bettega, C. Picart, Surface delivery of tunable doses of BMP-2 from an adaptable polymeric scaffold induces volumetric bone regeneration, Biomaterials 104 (2016) 168–181.
[22] J.A. McGovern, M. Griffin, D.W. Hutmacher, Animal models for bone tissue engineering and modelling disease, Disease models & mechanisms 11 (4) (2018).
[23] T. Crouzier, L. Fourel, T. Boudou, C. Albiges-Rizo, C. Picart, Presentation of BMP-2 from a soft biopolymeric film unveils its activity on cell adhesion and migration, Adv. Mater. 23 (12) (2011) H111–H118.
[24] T. Crouzier, K. Ren, C. Nicolas, C. Roy, C. Picart, Layer-by-Layer films as a biomimetic reservoir for rhBMP-2 delivery: controlled differentiation of myoblasts to osteoblasts, Small 5 (5) (2009) 598–608.
[25] R. Guillot, F. Gilde, P. Becquart, F. Sailhan, A. Lapeyrere, D. Logeart-Avramoglou, C. Picart, The stability of BMP loaded polyelectrolyte multilayer coatings on titanium, Biomaterials 34 (23) (2013) 5737–5746.
[26] T. Crouzier, F. Sailhan, P. Becquart, R. Guillot, D. Logeart-Avramoglou, C. Picart, The performance of BMP-2 loaded TCP/HAP porous ceramics with a polyelectrolyte multilayer film coating, Biomaterials 32 (30) (2011) 7543–7554.
[27] C. Kunert-Keil, H. Richter, I. Zeidler-Rentzsch, I. Bleeker, T. Gredes, Histological comparison between laser microtome sections and ground specimens of implant-containing tissues, Ann. Anat. 222 (2019) 153–157.
[28] J.K. Stembirek, M. Kyllar, I. Putnova, L. Stehlik, M. Buchtova, The pig as an experimental model for clinical craniofacial research, Lab. Anim 46 (2012) 269–279, 46 (2012) 269-279.
[29] B. Saka, A. Wree, L. Anders, K.K. Gundlach, Experimental and comparative study of the blood supply to the mandibular cortex in Gottingen minipigs and in man, J. Cranio-Maxillo-Fac. Surg. 30 (4) (2002) 219–225.
[30] Z. Sun, K.S. Kennedy, B.C. Tee, J.B. Damron, M.J. Allen, Establishing a critical-size mandibular defect model in growing pigs: characterization of spontaneous healing, J. Oral Maxillofac. Surg. 72 (9) (2014) 1852–1868.
[31] J.L. Ma, J.L. Pan, B.S. Tan, F.Z. Cui, Determination of critical size defect of minipig mandible, J Tissue Eng Regen Med 3 (8) (2009) 615–622.
[32] F.A. Probst, R. Fliefel, E. Burian, M. Probst, M. Eddicks, M. Cornelsen, C. Riedl, H. Seitz, A. Aszodi, M. Schieker, S. Otto, Bone regeneration of minipig mandibular defect by adipose derived mesenchymal stem cells seeded tri-calcium phosphate-poly(D,L-lactide-co-glycolide) scaffolds, Sci. Rep. 10 (1) (2020) 2062.
[33] D.W. Hutmacher, Scaffolds in tissue engineering bone and cartilage, Biomaterials 21 (24) (2000) 2529–2543.
[34] A. Cipitria, C. Lange, H. Schell, W. Wagermaier, J.C. Reichert, D.W. Hutmacher, P. Fratzl, G.N. Duda, Porous scaffold architecture guides tissue formation, J. Bone Miner. Res. 27 (6) (2012) 1275–1288.
[35] A. Cipitria, W. Wagermaier, P. Zaslansky, H. Schell, J.C. Reichert, P. Fratzl, D.W. Hutmacher, G.N. Duda, BMP delivery complements the guiding effect of scaffold architecture without altering bone microstructure in critical-sized long bone defects: a multiscale analysis, Acta Biomater. 23 (2015) 282–294.
[36] J.E. Bergsma, W.C. de Bruijn, F.R. Rozema, R.R. Bos, G. Boering, Late degradation tissue response to poly(L-lactide) bone plates and screws, Biomaterials 16 (1) (1995) 25–31.
[37] C. Garot, G. Bettega, C. Picart, Additive manufacturing of material Scaffolds for bone regeneration: toward application in the clinics, Adv. Funct. Mater. (2020) 2006967, n/a(n/a).
[38] M. Kuterbekov, P. Machillot, P. Lhuissier, C. Picart, A.M. Jonas, K. Glinel, Solvent-free preparation of porous poly(l-lactide) microcarriers for cell culture, Acta Biomater. 75 (2018) 300–311.
[39] S. Farah, D.G. Anderson, R. Langer, Physical and mechanical properties of PLA, and their functions in widespread applications - a comprehensive review, Adv. Drug Deliv. Rev. 107 (2016) 367–392.
[40] J.D. Boerckel, Y.M. Kolambkar, K.M. Dupont, B.A. Uhrig, E.A. Phelps, H.Y. Stevens, A.J. Garcia, R.E. Guldberg, Effects of protein dose and delivery system on BMP-mediated bone regeneration, Biomaterials 32 (22) (2011) 5241–5251.
[41] S.D. Boden, J. Kang, H. Sandhu, J.G. Heller, Use of recombinant human bone morphogenetic protein-2 to achieve posterolateral lumbar spine fusion in humans: a prospective, randomized clinical pilot trial: 2002 Volvo Award in clinical studies, Spine 27 (23) (2002) 2662–2673.
[42] A.F. Kamal, O.S.H. Siahaan, J. Fiolin, Various dosages of BMP-2 for management of massive bone defect in Sprague Dawley rat, Arch Bone Jt Surg 7 (6) (2019) 498–505.
[43] E.L. Durham, R.N. Howie, S. Hall, N. Larson, B. Oakes, R. Houck, Z. Grey, M. Steed, A.C. LaRue, R. Muise-Helmericks, J. Cray, Optimizing bone wound healing using BMP2 with absorbable collagen sponge and Talymed nanofiber scaffold, J. Transl. Med. 16 (1) (2018) 321.
[44] P. Sun, J. Wang, Y. Zheng, Y. Fan, Z. Gu, BMP2/7 heterodimer is a stronger inducer of bone regeneration in peri-implant bone defects model than BMP2 or BMP7 homodimer, Dent. Mater. J. 31 (2) (2012) 239–248.
[45] J. Wang, Y. Zheng, J. Zhao, T. Liu, L. Gao, Z. Gu, G. Wu, Low-dose rhBMP2/7 heterodimer to reconstruct peri-implant bone defects: a micro-CT evaluation, J. Clin. Periodontol. 39 (1) (2012) 98–105.
[46] M.H. Pelletier, R.A. Oliver, C. Christou, Y. Yu, N. Bertollo, H. Irie, W.R. Walsh, Lumbar spinal fusion with beta-TCP granules and variable Escherichia coli-derived rhBMP-2 dose, Spine J. 14 (8) (2014) 1758–1768.
[47] M. Hoshino, T. Egi, H. Terai, T. Namikawa, K. Takaoka, Repair of long intercalated rib defects using porous beta-tricalcium phosphate cylinders containing recombinant human bone morphogenetic protein-2 in dogs, Biomaterials 27 (28) (2006) 4934–4940.
[48] R. Guillot, I. Pignot-Paintrand, J. Lavaud, A. Decambron, E. Bourgeois, V. Josserand, D. Logeart-Avramoglou, E. Viguier, C. Picart, Assessment of a polyelectrolyte multilayer film coating loaded with BMP-2 on titanium and PEEK implants in the rabbit femoral condyle, Acta Biomater. 36 (2016) 310–322.
[49] F. Gilde, L. Fourel, R. Guillot, I. Pignot-Paintrand, T. Okada, V. Fitzpatrick, T. Boudou, C. Albiges-Rizo, C. Picart, Stiffness-dependent cellular internalization of matrix-bound BMP-2 and its relation to Smad and non-Smad signaling, Acta Biomater. 46 (2016) 55–67.